A&A 491, 747–754 (2008)
DOI: 10.1051/0004-6361:200810482

Astronomy & Astrophysics

The CO line SED and atomic carbon in IRAS F10214+4724⋆

Y. Ao[1,2], A. Weiß[2], D. Downes[3], F. Walter[4], C. Henkel[2], and K. M. Menten[2]

[1] Purple Mountain Observatory, Chinese Academy of Sciences, Nanjing 210008, PR China
e-mail: ypao@pmo.ac.cn
[2] MPIfR, Auf dem Hügel 69, 53121 Bonn, Germany
[3] IRAM, Domaine Universitaire, 38406 St-Martin-d'Hères, France
[4] MPIA, Königstuhl 17, 69117 Heidelberg, Germany

Received 30 June 2008 / Accepted 2 October 2008

ABSTRACT

Using the IRAM 30 m telescope and the Plateau de Bure interferometer we have detected the C I($^3P_2 \rightarrow {}^3P_1$) and the CO 3–2, 4–3, 6–5, 7–6 transitions as well as the dust continuum at 3 and 1.2 mm towards the distant luminous infrared galaxy IRAS F10214+4724 at $z = 2.286$. The C I($^3P_2 \rightarrow {}^3P_1$) line is detected for the first time towards this source and IRAS F10214+4724 now belongs to a sample of only 3 extragalactic sources at any redshift where both of the carbon fine structure lines have been detected. The source is spatially resolved by our C I($^3P_2 \rightarrow {}^3P_1$) observation and we detect a velocity gradient along the east-west direction. The CI line ratio allows us to derive a carbon excitation temperature of 42^{+12}_{-9} K. The carbon excitation in conjunction with the CO ladder and the dust continuum constrain the gas density to $n(H_2) = 10^{3.6-4.0}$ cm^{-3} and the kinetic temperature to $T_{kin} = 45-80$ K, similar to the excitation conditions found in nearby starburst galaxies. The rest-frame 360 μm dust continuum morphology is more compact than the line emitting region, which supports previous findings that the far infrared luminosity arises from regions closer to the active galactic nucleus at the center of this system.

Key words. galaxies: formation – galaxies: high-redshift – galaxies: individual: IRAS F10214+4724 – galaxies: ISM – galaxies: active – infrared: galaxies

1. Introduction

Recent submm- and mm-wavelength dust continuum surveys from SCUBA at the JCMT (Ivison et al. 2000; Coppin et al. 2006) and MAMBO at the IRAM 30 m telescope (Bertoldi et al. 2007) have revealed a population of so-called submm galaxies (SMGs) at high redshift with far infrared (FIR) luminosities comparable to or higher than those of local Ultraluminous Infrared Galaxies (ULIRGs). Spectroscopic follow-up studies of SMGs in the optical regime suggest that the volume density of these sources increases by three orders of magnitude out to $z \sim 2$ (Chapman et al. 2005) and, in contrast to the local Universe, ULIRGs could thus dominate the total bolometric luminosity from star formation at early epochs.

About 50 of these high-z, luminous infrared (IR) galaxies have been detected in CO emission lines (see Solomon & Vanden Bout 2005, for a review), and a significant fraction have been imaged in CO with the IRAM Plateau de Bure Interferometer (PdBI) by Greve et al. (2005). Such observations provide important constraints on their molecular gas masses, kinematics and dynamical masses. For a few of these sources multi-transition studies of CO, C I and HCN have been presented (Weiß et al. 2005b, 2007; Alloin et al. 2007), which focus on the excitation properties of these massive gas reservoirs at high redshift.

IRAS F10214+4724 (F10214 hereafter) was the first high-z source detected in CO (Brown & Vanden Bout 1991; Solomon et al. 1992) and has been observed in the CO(3–2) line by many authors (see Radford et al. 1996, for a summary), and the CO(4–3) (Brown & Vanden Bout 1992), CO(6–5) (Solomon et al. 1992) as well as the C I($^3P_1 \rightarrow {}^3P_0$) transitions (Weiß et al. 2005a). CO(1–0) was tentatively detected (Tsuboi & Nakai 1992, 1994), but not confirmed by Barvainis (1995). An upper limit on the C I($^3P_2 \rightarrow {}^3P_1$) line was reported by Papadopoulos (2005). The gas distribution was also investigated in detail by the high angular resolution observations in CO(3–2) of Downes et al. (1995) and Scoville et al. (1995).

In this paper we present new measurements of the CO(3–2), CO(4–3), CO(6–5) and CO(7–6) lines and the first successful detection of the higher level fine structure line of atomic carbon, together with the continuum emission at 3 mm and 1.2 mm towards F10214.

2. Observations

2.1. IRAM PdBI observations

We observed the CO $J = 3-2$ rotational line and the C I($^3P_2 \rightarrow {}^3P_1$) fine structure line with the PdBI in the compact D configuration during 8 nights in 2004. The dual frequency setup was used, and assuming a redshift, z, of 2.2854 the receivers were tuned to the redshifted CO(3–2) frequency of 105.252 GHz in the 3 mm band and the frequency of the redshifted C I($^3P_2 \rightarrow {}^3P_1$) transition at 246.345 GHz in the 1.2 mm band (both upper side band tunings). During this run the weather was poor and the performance of the old receivers in the 1.2 mm band was unsatisfactory, thus only the 3 mm data was useful, yielding an equivalent 6-antenna on-source integration time of 17 h for CO(3–2) with an average system temperature of 180 K. Baselines ranged from

⋆ Based on observations carried out with the IRAM Plateau de Bure Interferometer. IRAM is supported by INSU/CNRS (France), MPG (Germany) and IGN (Spain).

15.5 to 112.6 m resulting in a synthesized beam of 6.5″ × 3.8″ (PA ~ 105° E of N) for natural weighting and 4.9″ × 3.2″ (PA ~ 92° E of N) for uniform weighting. The spectral correlator covers ~1590 km s^{-1} with a velocity resolution of 2 km s^{-1}.

The C I(^{3}P$_2$ → ^{3}P$_1$) line was reobserved with the new PdBI receivers on December 25th, 2007 under good weather conditions in C configuration. Both polarizations were tuned to the redshifted C I(^{3}P$_2$ → ^{3}P$_1$) line, giving a velocity coverage of ~1210 km s^{-1} (1 GHz band width) and a velocity resolution of 3 km s^{-1}. Baselines ranged from 16.3 to 175.3 m yielding a synthesized beam of 1.12″ × 0.97″ (PA ~ 4° E of N) for natural weighting. The on-source integration time for this run is ~5.5 h with a typical system temperature of 200 K.

Amplitudes were calibrated using 3C 84, 3C 454.3, 0420-014, CRL618, and MWC 349. For phase calibration we observed the nearby calibrators 0923+392 and 0955+476. The data were processed with the programs from GILDAS software packages and the final data cubes have noise levels of 1.9 mJy per beam (for uniform weighting) at 20 km s^{-1} and 2.7 mJy per beam at 30 km s^{-1} resolution for the 3 mm and 1.2 mm line cubes, respectively. The noise levels of the final continuum maps, which were computed by averaging the line free channels, are 0.17 mJy per beam (for natural weighting) at 3 mm and 0.7 mJy per beam at 1.2 mm, respectively. We estimate the flux density scale to be accurate to about 10% at 3 mm and 20% at 1.2 mm.

2.2. IRAM 30 m observations

The IRAM 30 m observations toward F10214 were carried out during the period between 2004 July and 2005 February. We used the A/B and C/D receiver combinations tuned to CO(3−2) (105.252 GHz, 3 mm band), CO(4−3) (140.330 GHz, 2 mm band), CO(6−5) (210.468 GHz, 1.3 mm band) and CO(7−6) (245.526 GHz, 1.2 mm band) lines, respectively. The beam sizes/antenna gains for increasing frequency are 23.4″/6.3 Jy K^{-1}, 17.5″/6.7 Jy K^{-1}, 11.7″/7.9 Jy K^{-1} and 10″/9.5 Jy K^{-1}, respectively. Typical system temperatures were about 120 K, 255 K, 240 K and 330 K for the four CO lines, respectively. The observations were done in wobbler switching mode, with a switching frequency of 0.5 Hz and a wobbler throw of 50″ in azimuth. Data were recorded using the 512 × 1 MHz filter banks for the 3 mm receivers (500 MHz total bandwidth), and the 256 × 4 MHz filter banks for the 2 and 1.3 mm receivers (1 GHz total bandwidth). The data were reduced with the CLASS software. We first omitted scans with distorted baselines, and only subtracted linear baselines from individual spectra, and then averaged all the useful scans. Finally, we smoothed the spectra to the velocity resolution of 34, 34, 40 and 30 km s^{-1}, respectively. The useful on-source integration times are 3.8, 5.9, 3.2 and 9.2 h for the four CO lines and the resulting rms noise values are 3.5, 4.0, 3.3 and 4.6 mJy, respectively.

3. Results

3.1. Neutral carbon line

The C I(^{3}P$_2$ → ^{3}P$_1$) line is detected towards F10214 for the first time. The integrated line flux is $I_{\mathrm{CI}(^3\mathrm{P}_2\rightarrow{}^3\mathrm{P}_1)}$ = 4.59 ± 0.66 Jy km s^{-1} which is consistent with the upper limit of 7 Jy km s^{-1} reported by Papadopoulos (2005). Together with the detection of the C I(^{3}P$_1$ → ^{3}P$_0$) line (Weiß et al. 2005a), F10214 is only the third extragalactic source, next to the Cloverleaf (Barvainis et al. 1997; Weiß et al. 2003) and M 82 (Stutzki et al. 1997), where both carbon lines have been detected. The resulting carbon line ratio, $L'_{\mathrm{CI}(^3\mathrm{P}_2\rightarrow{}^3\mathrm{P}_1)}/L'_{\mathrm{CI}(^3\mathrm{P}_1\rightarrow{}^3\mathrm{P}_0)}$, is 0.84 ± 0.19. The C I(^{3}P$_2$ → ^{3}P$_1$) line width is 182 ± 30 km s^{-1} which agrees well with the linewidth derived from the CO(3−2) and CO(6−5) lines and the lower carbon line (see Sect. 3.2).

The C I(^{3}P$_2$ → ^{3}P$_1$) spectral line data are presented as channel maps in Fig. 1. The emission peaks move from west to east for increasing velocities which indicates that the gas rotates along the east-west direction. This rotation is also seen in the velocity field of the C I(^{3}P$_2$ → ^{3}P$_1$) line, which is presented as a color map in Fig. 2 (right). In the same figure we show the contours of the integrated line intensity. From the line intensity map it is apparent that the C I(^{3}P$_2$ → ^{3}P$_1$) distribution is spatially resolved. The deconvolved full width to half maximum (FWHM) source size is <0.7″ and 1.4″ ± 0.1″ along the minor and major axis respectively, and the position angle is 84° (E of N). This morphology is similar to the arc-like lensed structure visible at 2.2 μm (Matthews et al. 1994; Graham & Liu 1995). The carbon distribution, however, does not show the additional compact 2.2 μm component about 3″ north of the arc which argues for differential lensing between the wavelengths of the near infrared (NIR) emission and those of the molecular gas. The C I(^{3}P$_2$ → ^{3}P$_1$) distribution is similar to the morphology derived from CO (Downes et al. 1995).

The 1.2 mm (restframe 360 μm) continuum map is shown in Fig. 2 (left). Interestingly, its distribution differs from the morphology seen in the carbon line. It it much more compact and the deconvolved FWHM source size is <0.7″. The continuum peaks at α(J2000) = 10$^{\mathrm{h}}$24$^{\mathrm{m}}$34$^{\mathrm{s}}$.56, δ(J2000) = +47°09′09″.8 (±0.1″) which agrees well with the peak of the C I(^{3}P$_2$ → ^{3}P$_1$) line. The 1.2 mm continuum flux is 9.9 ± 1.2 mJy, in good agreement with the flux of 9.6 ± 1.4 mJy reported by Downes et al. (1992) at the same wavelength. The peak intensity is 8.3 mJy beam^{-1}, which suggests the source is slightly resolved spatially.

3.2. CO lines

Our PdBI CO(3−2) line observations are represented as channel maps in Fig. 3 and the moment maps in the right panel of Fig. 4. The 3 mm continuum (rest frame 930 μm) is detected for the first time and we find an integrated flux density of 0.58 ± 0.24 mJy and an emission peak at a 3σ level. To achieve higher sensitivity, natural weighting was used to create the continuum map (Fig. 4 left). Although the signal is only detected at 3σ significance, the good positional agreement with the 1.2 mm peak supports the reliability of our detection. The 3 mm continuum as well as the integrated line distribution remain unresolved in our 4.9″ × 3.3″ and 6.5″ × 3.8″ beams, consistent with the size estimates from the higher resolution 1.2 mm data. The emission centroids of the integrated CO(3−2) and the continuum distributions coincide well with the peak position derived at 1.2 mm. Inspection of individual channel maps shows that also the CO(3−2) emission has a velocity gradient along east-west direction, consistent with the rotation seen in C I(^{3}P$_2$ → ^{3}P$_1$). The CO(3−2) velocity field is shown in Fig. 4 (right), where the ordered velocity gradient is obvious along the east-west direction. The spatial separation between the centroids of the blue and red emission in the channel maps is about 2″, somewhat higher than, but consistent with, the extent of the C I(^{3}P$_2$ → ^{3}P$_1$) emission. This further suggests that the molecular gas detected in CO is cospatial with the gas detected in the carbon line.

Our 30 m CO spectra are presented in Fig. 5. To reduce the uncertainty in the CO line profiles we use all CO spectra to

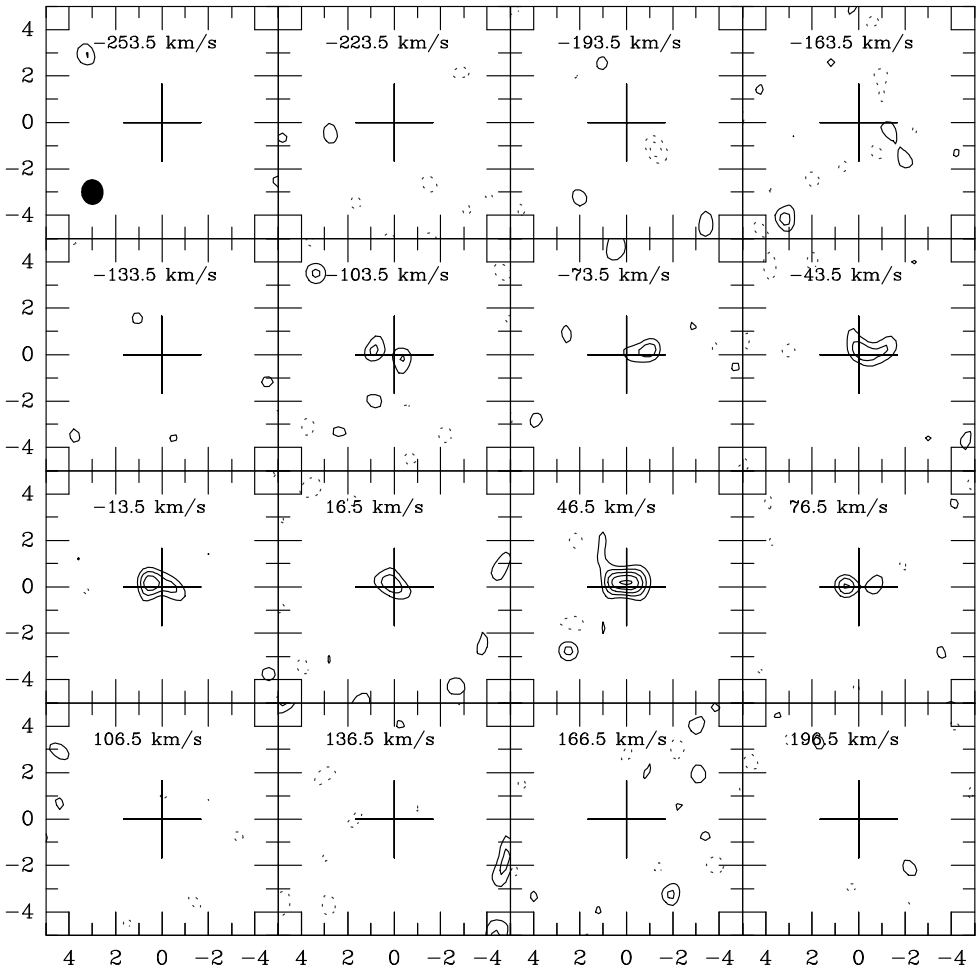

Fig. 1. Channel maps of the C I($^3P_2 \rightarrow {}^3P_1$) line of F10214 after subtracting the continuum. The contours are −3, −2, 2, 3, 4, 5, 6, 7 × 2.7 mJy beam^{-1} (1σ), with a synthesized beam of 1.12″ × 0.97″, which is shown in *the lower left corner* of the first panel. The maps are centered on the position shown as a cross (α(J2000) = $10^h24^m34\overset{s}{.}56$, δ(J2000) = +47°09′09.″8), here and in subsequent figures.

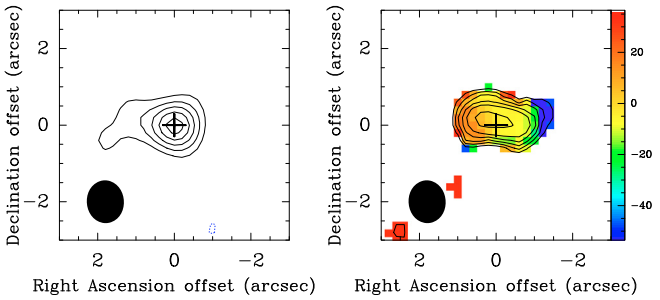

Fig. 2. *Left panel*: contour map of the 1.2 mm continuum towards F10214, which was created from the line free channels. Contours are −3, 3, 5, 7, 9, 11 × 0.7 mJy beam^{-1} (1σ). *Right panel*: contour map of the C I($^3P_2 \rightarrow {}^3P_1$) line integrated intensity towards F10214 after subtracting the continuum overlaid by the velocity field in color map. Contours are −3, 3, 6, 9, 12, 15, 20 × 0.081 Jy km s^{-1} beam^{-1} (1σ). A synthesized beam of 1.12″ × 0.97″ is shown in *the lower left corner* of the figures.

obtain an average line profile (first panel of Fig. 5). A Gaussian fit to this spectrum yields a line width of 246 ± 10 km s^{-1}, and redshift of 2.28562 ± 0.00004. Line parameters of individual lines were obtained from Gaussian fits keeping the linewidth fixed to the value of the average spectrum. The line parameters are summarized in Table 1. The averaged CO line width is higher than the values from both carbon lines and the CO(3−2) line, which is mainly because the CO(4−3) and CO(7−6) appear to have broader line profiles. which is mainly because the CO(4−3) and CO(7−6) lines appear to have broader profiles. More specifically both CO(3−2) spectra are somewhat asymmetric with the blue line wing being more prominent than the red wing (see Fig. 5). This asymmetry is also marginally visible in both CI profiles but not in the higher-J CO transitions. Although the effect is not very pronounced it could indicate the presence of cold foreground material at low density with sufficient optical depth to affect the low-J CO and CI lines but not the high J CO transitions which have much higher critical densities. One could also argue that only the low-J CO and CI lines arise cospatially while the high-J CO transitions trace a different volume. The later explanation, however, ignores that a volume that emits in the high-J CO transitions will always be bright in the low-J lines too.

The CO(3−2) flux of the spectrum from the 30 m telescope is 3.80 ± 0.45 Jy km s^{-1}, which is in agreement with previous results (see Radford et al. 1996, for a summary) and also with our high S/N PdBI observation which gives 3.40 ± 0.19 Jy km s^{-1}.

Previous observations of the CO(4−3) and CO(6−5) lines have been reported by Brown & Vanden Bout (1992) and Solomon et al. (1992). Our CO(4−3) integrated intensity is 5.32 ± 0.51 Jy km s^{-1}, which is only about one third of the value given by Brown & Vanden Bout (1992). Considering the high

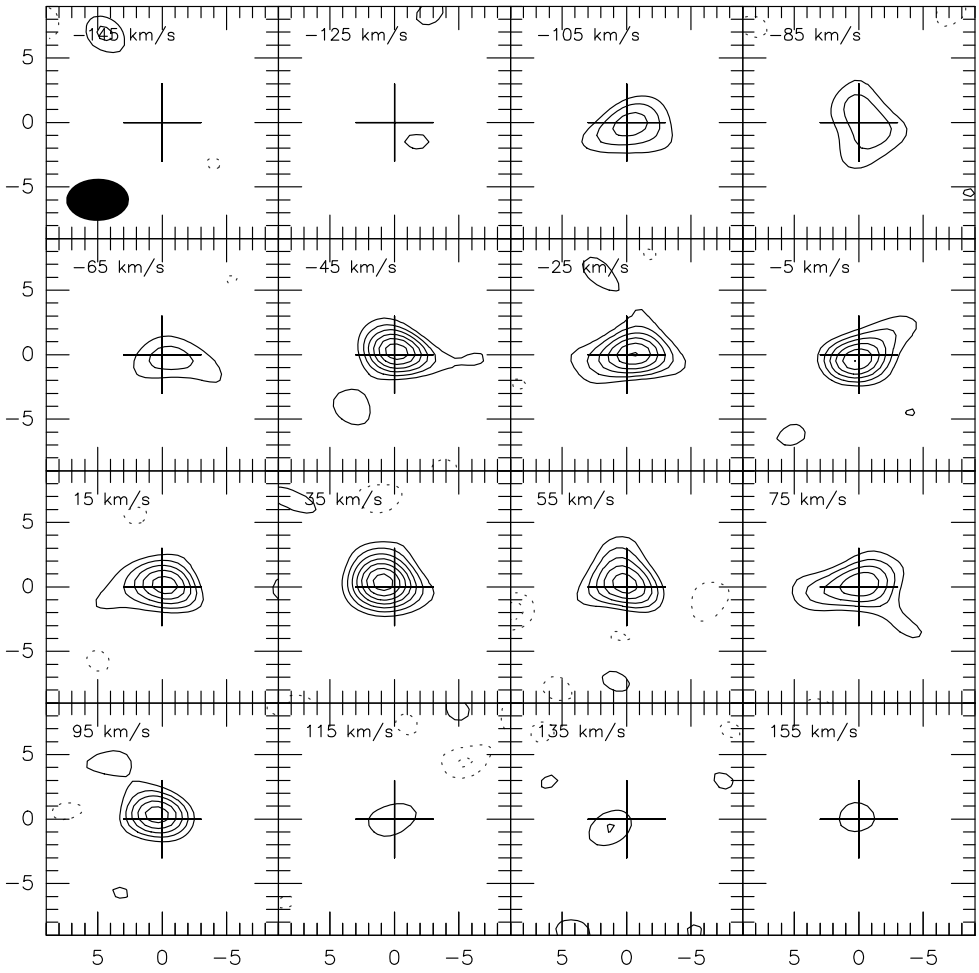

Fig. 3. CO(3−2) channel maps of F10214 after subtracting the continuum. The contours are −3, −2, 2, 3, 4, 5, 6, 7, 8, 9 × 1.9 mJy beam^{-1} (1σ), with a synthesized beam of 4.9″ × 3.3″, which is shown in *the lower left corner* of the first panel.

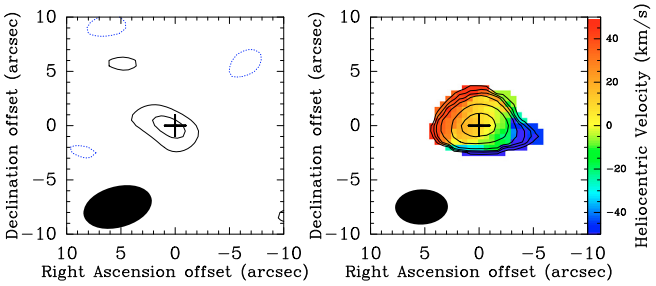

Fig. 4. *Left panel*: contour map of the 3 mm continuum towards F10214, which was created from the line free channels. Contours are −2, 2, 3 × 0.17 mJy beam^{-1} (1σ). *Right panel*: contour map of the CO(3−2) line integrated intensity towards F10214 after subtracting the continuum overlaid by the velocity field in color map. Contours are −3, 3, 9, 15, 30, 50 × 0.038 Jy km s^{-1} beam^{-1} (1σ). The synthesized beams of 6.5″ × 3.8″ and 4.9″ × 3.3″ are shown in *the lower left corner* of the figures.

quality of our new spectrum and the flux densities observed for the other CO transitions we consider our new CO(4−3) measurement to be more reliable. Our CO(6−5) line integrated intensity is 7.09 ± 0.47 Jy km s^{-1}, which is consistent with the previous value by Solomon et al. (1992).

Our detection of the CO(7−6) transition is the first published detection of this transition towards this source. Its line integrated intensity is 5.43 ± 0.56 Jy km s^{-1}. Therefore, our observations constrain the peak of the CO line spectral energy distribution (SED; i.e. the integrated line flux densities versus the rotational quantum number) in F10214 to be at the CO(6−5) line. The CO line SED including most of the CO observations from the literature and the present study is shown in Fig. 6.

4. Discussion

4.1. CO gas excitation

To investigate the CO excitation we here use a one-component large velocity gradient (LVG) analysis as described by Weiß et al. (2007) adopting a fixed CO abundance per velocity gradient of [CO]/(dv/dr) = 1 × 10^{-5} pc (km s^{-1})$^{-1}$. As discussed before, the line profiles may suggest a more complex gas excitation (for an example of a two component model, see the case of APM08279+5255 discussed by Weiß et al. 2007). Since, however, the differences in the line profiles are not very pronounced and more likely explained by foreground absorption rather than a 2 component excitation we use here for simplicity a one-component model which yields the average gas excitation in F10214. From the LVG model we can limit the allowed range for the H_2 density to $10^{3.3-4.2}$ cm^{-3}. The kinetic temperature of the gas, however, is poorly constrained. This is shown in Fig. 7 where we show the χ^2 distribution of the $T_{\rm kin}$−n(H_2) parameter space of the CO LVG models.

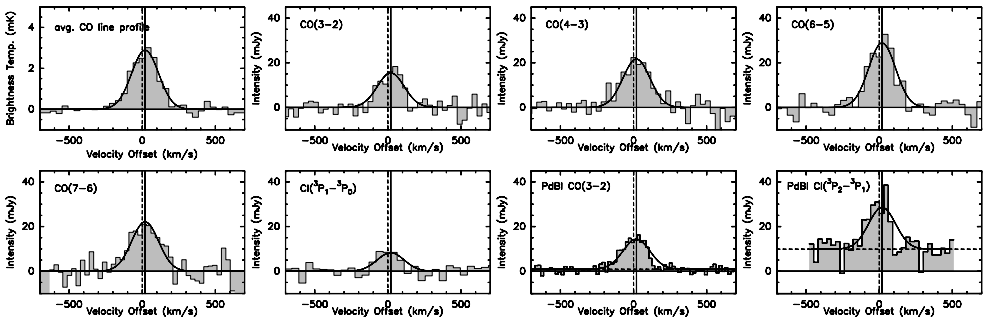

Fig. 5. Spectra of the averaged profile and the CO 3–2, 4–3, 6–5, 7–6, C I($^3P_1 \rightarrow {}^3P_0$) and C I($^3P_2 \rightarrow {}^3P_1$) lines towards F10214. The results from the PdBI are shown in the two panels at *the lower right*. All lines are fitted and Gaussian fits are shown as continuous lines for which the FWHM line width and the central velocity are fixed to the value determined from the averaged CO profile. The dashed horizontal lines in the PdBI spectra show the dust continuum levels. The zero and Gaussian fitted velocities from the averaged CO profile are shown as dashed vertical lines. The C I($^3P_1 \rightarrow {}^3P_0$) spectrum is taken from Weiß et al. (2005a).

Table 1. Observed CO and C I line parameters towards F10214.

Line	Telescope	$\nu_{\rm obs}$ [GHz]	$S_\nu{}^a$ [mJy]	$\Delta V_{\rm FWHM}{}^b$ [km s^{-1}]	I^a [Jy km s^{-1}]	V^b [km s^{-1}]	$L'/10^{10}{}^c$ [K km s^{-1} pc^2]
avg. profile	IRAM 30 m	...	...	246 ± 10	...	20 ± 4	...
CO(3–2)	IRAM 30 m	105.25230	15.5 ± 3.5	174 ± 23	3.80 ± 0.45	25 ± 11	10.83 ± 1.28
CO(3–2)	PdBI	105.25160	13.5 ± 0.6	224 ± 12	3.40 ± 0.19	4 ± 4	9.70 ± 0.54
CO(4–3)	IRAM 30 m	140.33020	21.7 ± 4.0	245 ± 28	5.32 ± 0.51	17 ± 11	8.53 ± 0.82
CO(6–5)	IRAM 30 m	210.46850	28.8 ± 3.3	203 ± 16	7.09 ± 0.47	20 ± 7	5.06 ± 0.34
CO(7–6)	IRAM 30 m	245.52621	22.1 ± 4.6	248 ± 30	5.43 ± 0.56	18 ± 14	2.84 ± 0.29
C I($^3P_1 \rightarrow {}^3P_0$)	IRAM 30 m	149.80235	8.3 ± 2.4	156 ± 26	2.03 ± 0.36	-5 ± 14	2.86 ± 0.51^d
C I($^3P_2 \rightarrow {}^3P_1$)	PdBI	246.34500	18.7 ± 2.3	182 ± 30	4.59 ± 0.66	-6 ± 10	2.39 ± 0.34

[a] The values are derived from Gaussian fits with the fixed line width and center velocity of the averaged CO line profile.
[b] The values are obtained from Gaussian fits to each spectrum. The velocity offsets are centered at a redshift of 2.2854 (Downes et al. 1995).
[c] We use a Λ cosmology with $H_0 = 73$ km s^{-1} Mpc^{-1}, $\Omega_\Lambda = 0.74$ and $\Omega_{\rm m} = 0.26$ (Spergel et al. 2007).
[d] The data are from Weiß et al. (2005a), but fitted with the fixed line width and central velocity.

For a gas kinetic temperature of $T_{\rm kin}$ = 45–80 K (as suggested from our carbon analysis and the dust model, see below) the allowed range for the gas density narrows to $n(H_2) = 10^{3.6-4.0}$ cm^{-3}. For these gas parameters the low-J CO lines are optically thick and thermalized which implies $L'_{\rm CO(1-0)} \approx L'_{\rm CO(3-2)}$. The LVG predicted integrated intensity of the CO(1–0) and CO(2–1) line emission are 0.37 ± 0.02 Jy km s^{-1} and 1.55 ± 0.05 Jy km s^{-1}, respectively. Within the uncertainties, the CO(1–0) flux from the LVG models is in agreement with the upper limit derived by Barvainis (1995).

4.2. Excitation temperature from C I

Recent studies in the Milky Way and nearby galaxies have shown that CO and C I have very similar distributions supporting the interpretation that their emission arises from the same gas volume (Fixsen et al. 1999; Ojha et al. 2001; Ikeda et al. 2002). The results from the carbon line and the CO(3–2) line by the PdBI also support that the molecular gas detected in CO is cospatial with the gas detected in the carbon line, as mentioned in Sect. 3. Thus, we can use our observed C I line ratio to obtain an independent estimate of the kinetic temperature via the C I excitation temperature to solve the ambiguity between the kinetic temperature and density arising from the CO LVG models. As discussed in Schneider et al. (2003) the carbon excitation temperature in the local thermodynamic equilibrium (LTE) can be derived from the C I line ratio via the formula $T_{\rm ex} = \frac{38.8}{\ln(\frac{2.11}{R})}$, where $R = \int T_{\rm mb}({\rm CI}(^3P_2 \rightarrow {}^3P_1))dv / \int T_{\rm mb}({\rm CI}(^3P_1 \rightarrow {}^3P_0))dv$, assuming that both carbon lines share the same excitation temperature and are optically thin. With our observed line ratio of 0.84 ± 0.19, we find $T_{\rm ex} = 42^{+12}_{-9}$ K.

4.3. C I abundance estimates

Using our estimate of the CO(1–0) line luminosity and the standard ULIRG factor $X_{\rm CO} = 0.8\ M_\odot$ (K km s^{-1} pc^2)$^{-1}$ (Downes & Solomon 1998), we find a molecular gas mass of (8.9 ± 1.0) × 10^{10} m^{-1} $M_\odot$ where m is the magnification factor by the gravitational lens. Using Eq. (2) in Weiß et al. (2005a) and our carbon excitation temperature of 42 K, the neutral carbon mass is $M_{\rm C\,I} = (3.7 \pm 0.7) \times 10^7$ m^{-1} $M_\odot$. This leads to a carbon abundance, [C I]/[H$_2$] = M[C I]/6M[H$_2$], of (6.9 ± 1.2) × 10^{-5}, in agreement with our previous results (Weiß et al. 2005a).

4.4. C I LVG models

To obtain an independent test on the optical depth of the C I lines in F10214 as well as on the LTE assumption used to derive the excitation temperature, we have also calculated LVG models for C I (Stutzki et al. 1997) using [C I]/(dv/dr) = 1.4 × 10^{-5} pc (km s^{-1})$^{-1}$. This abundance per velocity gradient corresponds to the C I abundance estimated above and a velocity gradient of (dv/dr) = 5 km s^{-1} pc^{-1}. For $T_{\rm kin}$ = 60 K and $n(H_2) = 10^{3.8}$ cm^{-3}, which provides a good fit to the observed CO SED, the resulting C I($^3P_2 \rightarrow {}^3P_1$)/C I($^3P_1 \rightarrow {}^3P_0$) line ratio is 0.8, which is consistent with our measurement of 0.84 ± 0.19. The LVG model predicts a C I($^3P_1 \rightarrow {}^3P_0$)/CO(3–2) line ratio of

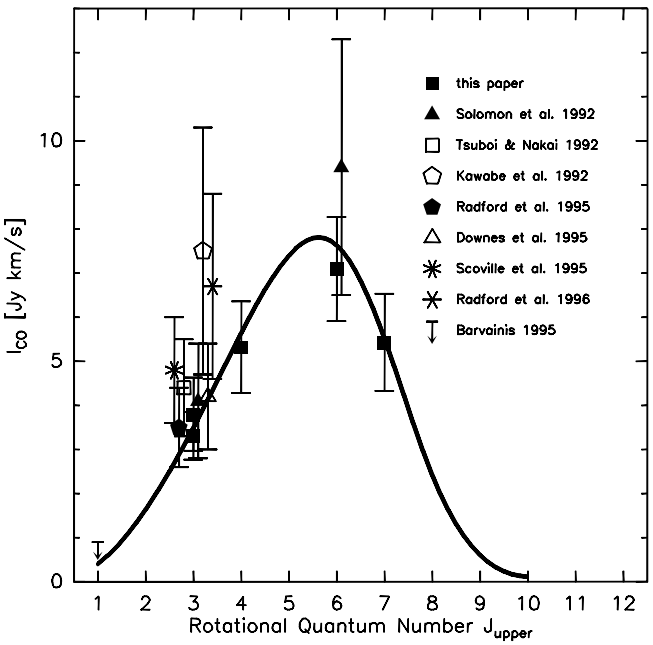

Fig. 6. Observed CO fluxes vs. rotational quantum number (CO line SED, filled squares) for F10214 fitted by the a single component LVG model with $n(H_2) = 10^{3.8}$ cm^{-3} and $T_{kin} = 60$ K, shown as a thick solid line. Other measurements, taken from the literatures, are marked by different symbols. For better visibility, previous data points for the 3−2 line are shown with small x-axis offsets.

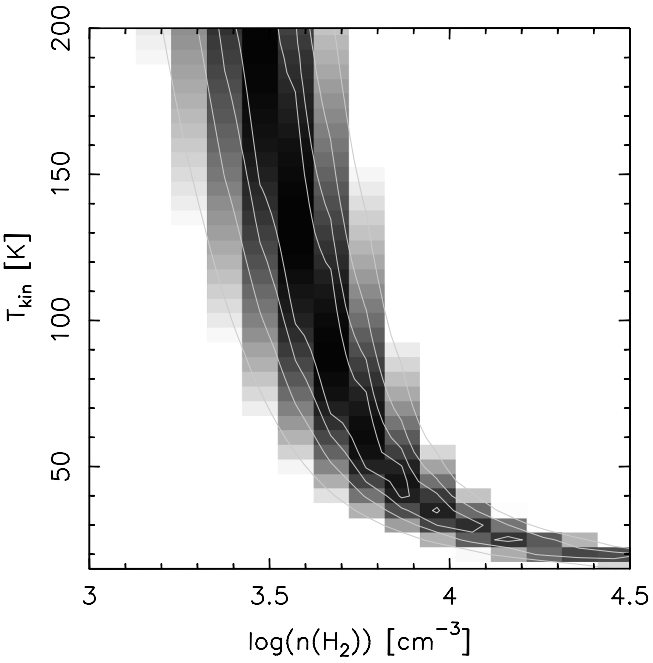

Fig. 7. Reduced χ^2 distribution for a single component LVG model fit to the observed line luminosity ratios (grey scale and white contours, contours: $\chi^2 = 0.5, 1, 2, 4$). The CO abundance per velocity gradient for the LVG models is $[CO]/(dv/dr) = 1 \times 10^{-5}$ pc (km s^{-1})$^{-1}$.

0.38, which is somewhat higher than the observed ratio of 0.26 ± 0.05. For this solution the excitation temperatures for the lower and upper carbon lines are 54 and 45 K, respectively. The optical depth in both transitions ranges from 0.5 to 0.6. Fine tuning of the gas parameters (e.g. a somewhat higher kinetic temperature of 70−80 K or a slightly lower carbon abundance per velocity gradient) will also bring the C I($^3P_1 \rightarrow {}^3P_0$)/CO(3−2) line ratio in agreement with the observations without significant changes of the excitation temperature or the optical depth of the lines. This implies that CO and CI LVG models with kinetic temperatures of ∼45−80 K provide reasonable estimates of the physical gas properties. This further suggests that the carbon lines in F10214 are indeed not far from LTE. Given the underlying assumptions, the single component LVG model for CO and CI gives a reasonable prediction for all CO and C I line intensities. This finding supports the view that the C I and CO emission arises from the same volume on galactic scales.

4.5. Size and magnification for CO and C I

The measured size of the C I emitting region in conjunction with the intrinsic line brightness temperatures for CO and C I allow us to estimate the lensing magnification factor and the intrinsic size of the gas distribution (see Downes et al. 1995). From our LVG models for C I and CO we find an intrinsic brightness temperature of 10−14 K and 38−47 K for C I($^3P_2 \rightarrow {}^3P_1$) and CO(3−2) respectively. Assuming our measured arc-length of 1.4″ also holds for the CO lines and adopting the method in Downes et al. (1995) to derive the lens magnification factor, this yields magnifications of 11−16 for the carbon line and 9−12 for CO(3−2), in agreement with the results in Downes et al. (1995). We note that the different magnifications between both lines simply reflect the uncertainties of the underlying brightness temperature and do not imply differential magnification. For a magnification factor of $m = 12$, the mean between both estimates, we derive an intrinsic source radius of ∼490 pc.

4.6. The dust continuum

We have included our new PdBI 3 mm and 1.2 mm measurements in the dust continuum analysis using a 2-component dust model as described in Weiß et al. (2007). Because the optically thin approximation for the dust emission does not necessarily hold at rest wavelength shorter than ∼100 μm for ULIRGs (Downes et al. 1993) we have used the approach described in Weiß et al. 2007: the flux density of the dust emission is related to the dust temperature, T_{dust}, and the apparent solid angle, Ω_{app} by the relation $S_\nu = [B_\nu(T_{dust}) - B_\nu(T_{bg})]\frac{(1-e^{-\tau_\nu})}{(1+z)^3}\Omega_{app}$, where S_ν is the observed (amplified) flux density and B_ν is the Planck function. The lens magnification factor is hidden in the apparent solid angle, Ω_{app}. The dust optical depth, τ_ν, is a property of the source itself and is independent of the effects of gravitational lensing: $\tau_\nu = \kappa_d(\nu_r) M_{dust,app}/D_A^2 \Omega_{app}$ where D_A is the angular distance of the source, $M_{dust,app}$ is the apparent dust mass and κ_d is the dust absorption coefficient. For the dust absorption coefficient, we adopt $\kappa_d(\nu) = 0.4\ (\nu_r/250\ \mathrm{GHz})^\beta$ cm^2 g^{-1}, where the dust emissivity index, $\beta = 2$.

The fit to all the data between 3 mm and 60 μm is shown in Fig. 8. The contribution of the non-thermal radio emission is negligible even at 3 mm. For the "cold" component, we find a dust temperature, T_{cold}, of 80 ± 10 K and a dust mass, M(cold dust), of 1.1×10^9 m^{-1} $M_\odot$(±25%). The warm component is poorly characterized as only two data points are available for the relevant frequency range. Our dust temperature for the cold component is in good agreement with the value given in Downes et al. (1992), but higher than the value of 55 K reported by Benford et al. (1999) although they adopted a slightly lower value of the dust emissivity index of 1.5. The physical size of the radius implied by our dust model is >350 pc for a magnification

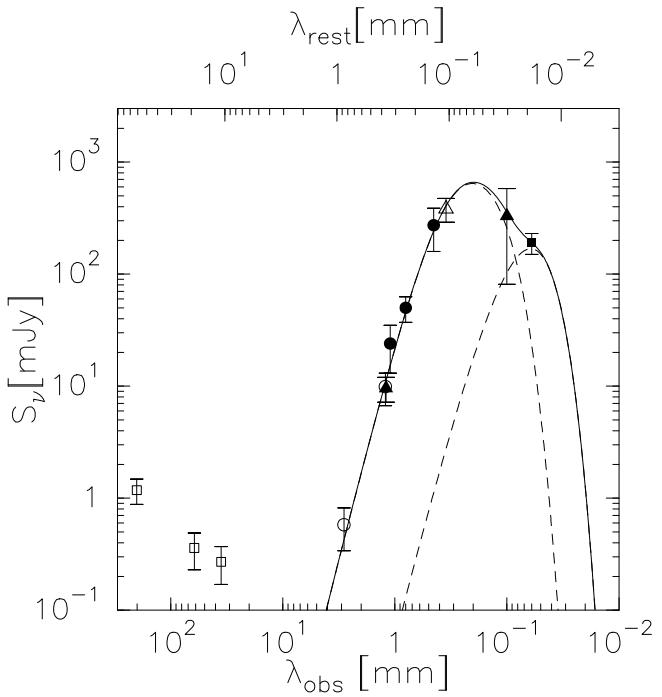

Fig. 8. Two component dust model for F10214. Displayed flux densities were taken from Lawrence et al. 1993 (20 cm, 6 cm and 3.6 cm, open squares), this work (3 mm and 1.2 mm, open circles), Downes et al. 1992 (1200, 100 μm, filled triangles), Rowan-Robinson et al. 1993 (1100, 800, 450 μm, filled circles), Benford et al. 1999 (350 μm, open triangle) and Rowan-Robinson et al. 1991 (60 μm, filled square). The dashed lines show the thermal dust continuum emission for 80 and 160 K dust components. The solid line is the total emission from both components. See Sect. 4.6 for the details of the dust models.

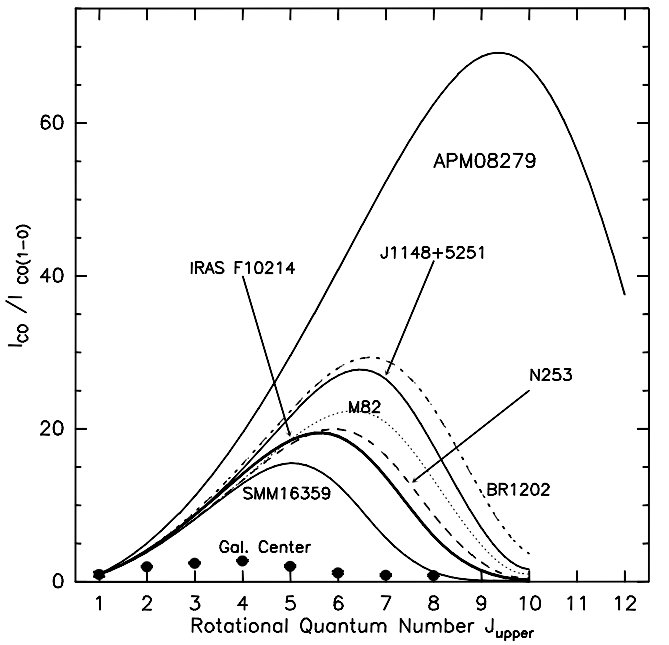

Fig. 9. Comparison of the CO line SEDs of selected local and high-z galaxies. The SEDs are shown for IRAS F10214+4724 (thick solid line, as shown in Fig. 6), APM 08279+5255 (z = 3.9, Weiß et al. 2007), BR 1202-0725 (z = 4.7, Riechers et al. 2006), SDSS J1148+5251 (z = 6.4, Bertoldi et al. 2003; Walter et al. 2003), the high-excitation component in the center of M 82 (Weiß et al. 2005c), NGC 253 center (Güsten et al. 2006), SMM J16359+6612 (z = 2.5, Weiß et al. 2005b) and the Galactic Center (solid circles, Fixsen et al. 1999). The CO line SEDs are normalized by their CO(1−0) flux density.

factor of 12. Much smaller real radii are inconsistent with the observed slope of the Rayleigh-Jeans tail of the dust SED due to the increasing optical depth of the dust emission. For the "cold" component, the dust optical depth at 100 μm of the rest frame is about 1.9. The dust temperature for the "cold" component provides an additional constraint on the kinetic temperature, which helps to narrow the ambiguity of the CO LVG models.

The small observed source size (<0.7″, i.e. <5800 pc, leads to a physical size of the radius of <240 pc for a magnification factor of 12) of the dust continuum emission at 1.2 mm implies that the FIR emission in F10214 arises from a different region than the C I and CO lines. This conclusion has already been reached by Downes et al. (1995) based on surface brightness arguments. The degree of compactness, however, is surprising because it is difficult to explain this structure in the context of existing lens models. Eisenhardt et al. (1996) suggested a magnification for the FIR emission region of 30 which translates into an even smaller FIR radius (<100 pc). Such small regions are inconsistent with our dust SED models unless we would adopt a dust emissivity spectral index $\beta > 2$ to compensate the higher optical depth arising from the more compact source size. We note, however, that our 1.2 mm dust continuum image shows a very faint east-west extension visible in the lowest contour shown in Fig. 2 (left). We therefore cannot rule out that we underestimate the size of the continuum region in our data. More sensitive 1.2 mm observations at ideally higher spatial resolution will be required to settle this issue. On the other hand, our high spatial resolution observations recover all of the 1.2 mm flux detected in single dish bolometer observations (Downes et al. 1992), so it appears unlikely that our observations miss large amounts of more extended emission. Therefore, the FIR emitting region may be compact enough that AGN heating could play a significant role even for the cooler dust at 80 K. This is also supported by the fact that the cold dust in F10214 is warmer than 40−60 K typically found in high-z QSOs (Benford et al. 1999; Beelen et al. 2006).

4.7. Comparison to other galaxies

Only a limited number of sources have been observed in a large enough number of CO lines to allow for a determination of the peak of their CO line SEDs (Fig. 9). From this figure it is apparent that F10214 has CO excitation characteristics similar to the centers of the nearby galaxies NGC 253 and M 82, and high-z galaxies like J1148+5251 and BR1202-0725 (for references, see the caption to Fig. 9). For all these sources, the peak of the CO SED occurs at the CO(6−5) or CO(7−6) lines. It is interesting to note, that for local starbursts such as M 82 the nuclear region is surrounded by large amounts of gas with lower CO excitation. This gas even dominates the emission in CO transitions below the CO(5−4) line (Walter et al. 2002; Weiß et al. 2005c). No such low excitation component is apparent in the CO SEDs of the high-z sources studied so far (Riechers et al. 2006). This implies that *all* the molecular gas and, in consequence, the starbursts arise from compact regions that dominate the (sub)mm emission. This is in agreement with the small equivalent radii determined from the dust and CO modelling, and also with the gas morphology of nearby ULIRGs where the CO emission often arises from compact, bright nuclear regions (Downes & Solomon 1998). So far, high-J CO observations in local ULIRGs have only been reported for Mrk 231 where the highest observed line is the

CO(6−5) transition (Papadopoulos et al. 2007). Also for this source the CO SED rises up to the CO(6−5) transition, which implies similar or even higher gas excitation compared to high-z FIR luminous galaxies.

While the CO excitation appears to be very similar for most active galaxies, there are two outstanding examples visible in Fig. 9: APM08279+5255 has a much higher CO excitation compared to all other sources. For this source, AGN heating and high gas densities have been suggested to be the main driver of the high gas excitation (Weiß et al. 2007). The submm galaxy SMM16359+6612, on the other hand, has the lowest CO excitation in the sample. For this source it was suggested that it is a merger that is not yet in the typical ULIRG stage as most of the gas may still be located in the overlap region between the merging galaxies (Kneib et al. 2004; Weiß et al. 2005b). For such a geometry the average gas densities (and therefore also the CO excitation as measured by the peak of the CO SED) is expected to be lower than for typical ULIRGs where almost all gas is located in the very central region of the merged galaxies.

5. Conclusion

Using the IRAM 30 m telescope and the PdBI we have detected the C I($^3P_2 \rightarrow {}^3P_1$), CO J = 3−2, 4−3, 6−5 and 7−6 transitions as well as the dust continuum at 3 and 1.2 mm towards IRAS F10214+4724. The C I($^3P_2 \rightarrow {}^3P_1$) line is detected for the first time towards this source and F10214 is now one out of only three extragalactic objects at any redshift where both carbon fine structure lines have been detected. The CI line ratio allows us to derive a carbon excitation temperature of 42^{+12}_{-9} K.

We have used the C I excitation temperature to narrow the temperature-density ambiguity in the LVG modeling for CO. The CO and C I lines together with the dust continuum constrain the gas density to $n(H_2) = 10^{3.6-4.0}$ cm^{-3} and the gas kinetic temperature to $T_{\rm kin}$ = 45−80 K. The gas excitation in F10214 is therefore similar to that found in the nuclei of nearby starburst galaxies. Given the underlying assumptions, the single component LVG model for CO and CI gives a reasonable prediction for all CO and C I line intensities. This finding supports the view that the C I and CO emission arises from the same volume on galactic scales.

The source is well resolved by our new C I($^3P_2 \rightarrow {}^3P_1$) line observation along the east-west direction, showing extended emission and a velocity gradient along the major axis, which is similar to the structure seen in CO. The major axis diameter in conjunction with the intrinsic brightness temperatures of CO and C I imply a gravitational magnification of ∼12, in agreement with previous results.

The continuum emission at 1.2 mm is more compact than the morphology of the C I($^3P_2 \rightarrow {}^3P_1$) line which shows that the FIR emitting region is smaller than the molecular gas distribution. We find a temperature of the cold dust of $T_{\rm cold} = 80 \pm 10$ K. The high dust temperature together with the compact morphology suggests that parts of the FIR emission could be due to heating of the central AGN.

Acknowledgements. We thank P. Cox for supporting this project through DDT observing time allocation for the new PdBI receivers which greatly improved our C I($^3P_2 \rightarrow {}^3P_1$) line spectrum. Y.A. acknowledges the financial support from Chinese Academy of Science for supporting his stay as a visiting scholar at MPIfR, when most of this work was done. Y.A. also acknowledges the support from NSFC grant 10733030. Finally, we appreciate the comments of the anonymous referee which improved our manuscript.

References

Alloin, D., Kneib, J., Guilloteau, S., & Bremer, M. 2007, A&A, 470, 53
Barvainis, R. 1995, AJ, 110, 1573
Barvainis, R., Maloney, P., Antonucci, R., & Alloin, D. 1997, ApJ, 484, 695
Beelen, A., Cox, P., Benford, D., et al. 2006, ApJ, 642, 694
Benford, D. J., Cox, P., Omont, A., Phillips, T. G., & McMahon, R. G. 1999, ApJ, 518, L65
Bertoldi, F., Cox, P., Neri, R., et al. 2003, A&A, 409, L47
Bertoldi, F., Carilli, C., Aravena, M., et al. 2007, ApJS, 172, 132
Brown, R. L., & Vanden Bout, P. A. 1991, AJ, 102, 1956
Brown, R. L., & Vanden Bout, P. A. 1992, ApJ, 397, L19
Chapman, S. C., Blain, A. W., Smail, I., & Ivison, R. J. 2005, ApJ, 622, 772
Coppin, K., Chapin, E. L., Mortier, A. M. J., et al. 2006, MNRAS, 372, 1621
Downes, D., & Solomon, P. M. 1998, ApJ, 507, 615
Downes, D., Radford, J. E., Greve, A., et al. 1992, ApJ, 398, L25
Downes, D., Solomon, P. M., & Radford, S. J. E. 1995, ApJ, 453, L65
Eisenhardt, P. R., Armus, L., Hogg, D. W., et al. 1996, ApJ, 461, 72
Fixsen, D. J., Bennett, C. L., & Mather, J. C. 1999, ApJ, 526, 207
Graham, J. R., & Liu, M. C. 1995, ApJ, 449, L29
Greve, T. R., Bertoldi, F., Smail, I., et al. 2005, MNRAS, 359, 1165
Güsten, R., Phillip, S. D., Weiß, A., & Klein, B. 2006, A&A, 454, 115
Ikeda, M., Oka, T., Tatematsu, K., Sekimoto, Y., & Yamamoto, S. 2002, ApJS, 139, 467
Ivison, R. J., Smail, I., Barger, A. J., et al. 2000, MNRAS, 315, 209
Kneib, J.-P., van der Werf, P. P., Kraiberg Knudsen, K., et al. 2004, MNRAS, 349, 1211
Krügel, E., & Siebenmorgen, R. 1994, A&A, 288, 929
Lawrence, A., Rowan-Robinson, M., Oliver, S., et al. 1993, MNRAS, 260, 28
Matthews, K., Soifer, B. T., Nelson, J., et al. 1994, ApJ, 420, L13
Ojha, R., Stark, A. A., Hsieh, H. H., et al. 2001, ApJ, 548, 253
Papadopoulos, P. P. 2005, ApJ, 623, 763
Papadopoulos, P. P., Isaak, K. G., & van der Werf, P. P. 2007 [arXiv:0706.0811]
Radford, S. J. E., Downes, D., Solomon, P. M., & Barrett, J. 1996, AJ, 111, 1021
Riechers, D. A., Walter, F., Carilli, C. L., et al. 2006, ApJ, 650, 604
Rowan-Robinson, M., Broadhurst, T., Oliver, S. J., et al. 1991, Nature, 351, 719
Rowan-Robinson, M., Efstathiou, A., Lawrence, A., et al. 1993, MNRAS, 261, 513
Schneider, N., Simon, R., Kramer, C., et al. 2003, A&A, 406, 915
Scoville, N. Z., Yun, M. S., Brown, R. L., & Vanden Bout, P. A. 1995, ApJ, 449, L109
Solomon, P. M., & Vanden Bout, P. 2005, ARA&A, 43, 677
Solomon, P. M., Downes, D., & Radford, S. J. E. 1992, ApJ, 398, L29
Spergel, D. N., Bean, R., Doré, O., et al. 2007, ApJS, 170, 377
Stutzki, J., Graf, U. U., Haas, S., et al. 1997, ApJ, 477, L33
Tsuboi, M., & Nakai, N. 1992, PASJ, 44, L41
Tsuboi, M., & Nakai, N. 1994, PASJ, 46, L179
Walter, F., Weiß, A., & Scoville, N. 2002, ApJ, 580, L21
Walter, F., Bertoldi, F., Carilli, C. L., et al. 2003, Nature, 424, 406
Weiß, A., Henkel, C., Downes, D., & Walter, F. 2003, A&A, 409, L41
Weiß, A., Downes, D., Henkel, C., & Walter, F. 2005a, A&A, 429, L25
Weiß, A., Downes, D., Walter, F., & Henkel, C. 2005b, A&A, 440, L45
Weiß, A., Walter, F., & Scoville, N. Z. 2005c, A&A, 438, 533
Weiß, A., Downes, D., Neri, R., et al. 2007, A&A, 467, 955